Additive Manufacturing 75 (2023) 103746

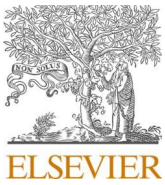

Contents lists available at ScienceDirect

Additive Manufacturing

journal homepage: www.elsevier.com/locate/addma

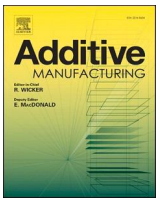

Microstructure evolution, phase formation, corrosion, and mechanical properties of stainless steel fabricated by extrusion-based sintering-assisted additive manufacturing

Fuji Wang [a], Siyao You [a], Dayue Jiang [b], Xiangyu Yuan [a], Rao Fu [a], Fuda Ning [b,*]

[a] School of Mechanical Engineering, Dalian University of Technology, Dalian 116023, China
[b] Department of Systems Science and Industrial Engineering, State University of New York (SUNY) at Binghamton, Binghamton, NY 13902, USA

ARTICLE INFO

Keywords:
Fused filament fabrication-debinding-sintering process
316 L stainless steel
Microstructural evolution
Phase formation
Corrosion and mechanical properties

ABSTRACT

In the domain of metal additive manufacturing (AM), a Fused Filament Fabrication (FFF), Debinding, and Sintering process that adopts polymer-based filaments with highly filled metal particles can be considered an economical solution to create large-size and refractory dense metal parts. Sintering, as a critical step, plays a critical role in determining the resultant microstructure uniformity of final parts. During sintering, the distribution and content of elements and phases in metal parts dictate the achieved material properties. In this work, the microstructure evolution during the entire sintering of FFF-printed 316L stainless steel (SS) parts was characterized and understood. The unique interlayer microstructures including interlayer pores and dislocation density were uncovered by characterizing grain morphologies of 316L SS at different sintering temperatures. Subsequently, the relationship between the chromium element segregation at the grain boundary and the formation of δ-ferrite phases was established through phase equilibrium simulation, phase characterization, and element analysis. Finally, the sintering temperature curve was optimized to achieve the direct preparation of single-phase austenitic SS with excellent pitting corrosion resistance and mechanical properties. The findings of this work will provide great insights into the mesoscale sintering behavior of FFF-built austenitic SS, paving new avenues for tailoring element/phase distribution to control the microstructure of metal alloys built by AM.

1. Introduction

Mainstream melting-based metal additive manufacturing (AM) technologies include powder bed fusion [1] and directed energy deposition [2]. These AM technologies exhibit manufacturing defects caused by melting and rapid solidification, high capital cost, and large energy consumptions [3]. Similar to binder jetting [4], Fused Filament Fabrication (FFF)-Debinding-Sintering process is an extrusion-based sintering-assisted AM process to create dense metal parts, as shown in Fig. 1. Printing step requires that polymer-based filaments with highly filled metal particles for deposition molding layer-by-layer. After printing, the polymetric binder is removed via the solvent, catalytic, or thermal debinding. Finally, the remaining porous metal materials will undergo high temperature sintering, which can be regarded as a combination of metal injection molding (MIM) and conventional AM processes. Compared with other metal AM technologies, metal FFF process does not involve high temperature gradient produced by melting-rapid cooling, which shows a great promise for the manufacture of metal alloys with high melting point [5] and large reflectivity [6].

Sintering plays an essential role in determining the microstructure, density, dimensional accuracy, and properties of the final metal parts [7]. For uniform microstructure, the sintering body should have low porosity with minimal defects and low brittle phase precipitation [8]. Recently, considerable investigations have been conducted in the characterization of FFF sintered metal alloys, such as stainless steel, pure copper, nickel-based superalloy, titanium alloy, and tungsten-based alloy, as summarized in Table 1.

The most extensively investigated metal in literature is 316L stainless steel (SS). Unlike the columnar grains presented by metal powder melting based AM technologies, the microstructure in FFF of 316L SS shows equiaxed austenitic grain morphologies with a more random orientation [13]. However, the inherent interlayer line defects along the building direction after printing affect the density distribution uniformity and porosity of the final part. At the atomic level, such defects also

* Corresponding author.
E-mail address: fning@binghamton.edu (F. Ning).

https://doi.org/10.1016/j.addma.2023.103746
Received 18 May 2023; Received in revised form 24 July 2023; Accepted 15 August 2023
Available online 18 August 2023

have potential effects on atomic diffusion and strain hardening behavior between interlayer particles, which directly leads to different phases and element distributions [11,23]. In a previous atomic simulation study of Ning et al. [24], chromium (Cr) enrichment at grain boundaries has been successfully identified. Related reports [7] indicate that the grain boundary phase could be $Cr_{23}C_6$. The formation of Cr-rich carbides could directly lead to Cr depleted zones at grain boundaries, which could exacerbate the potential risk of intergranular corrosion [7]. On the other hand, the FFF of 316L SS is mostly duplex austenitic stainless steel (mixed with less δ-ferrites) [10,13,25]. When the content of δ-ferrite exceeds 5 %, the staggered δ-ferrite grid structure will reduce the pitting corrosion resistance [26]. For other application scenarios, the content of δ-ferrite in non-magnetic materials should be less than 0.1 % [27]. However, related reports state that δ-ferrite is known to improve the ductility, toughness, and thermal cracking resistance of stainless steel [28,29]. For pressurizer surgeline pipes of pressure water reactors, the δ-ferrite content in austenitic SS welds must be greater than 5 % to improve weld mechanical properties [30]. From the perspective of crystal orientation relationships, the presence of δ-ferrite in 316L SS can also enhance dislocation mobility, greater work hardening, and higher ductility [31]. Therefore, it is necessary to control δ-ferrite content in 316L SS with advanced technologies to adapt to its increasing engineering applications in marine, nuclear, and chemical industries.

For 316L SS fabricated by FFF process, existing studies mostly focus on the microstructure-property correlation, enabling readers to have a preliminary understanding of the microscopic sintering behavior of 316L SS. However, the microstructure morphology is highly localized and temperature-dependent, and its evolution mechanism with sintering time requires further exploration. Anisotropy exists in FFF process due to the nature of heterogeneous distribution of particles and pores induced while it is commonly believed MIM results in relatively isotropic behaviors [32]. The existing knowledge of MIM could be misleading and non-conservative if it is directly applied to understand FFF for 316L SS fabrication. A comprehensive understanding of the phase formation of 316L SS during FFF process is still lacking. Especially for non-stationary second phases like δ-ferrite, its formation is sensitive to the microstructure uniformity and temperature. Wang et al. [13] attempted to combine HIP with FFF to improve the densification, microstructure, and mechanical properties of 316L SS. This method of combining sintering process with post-treatment has extremely important reference for our work.

In this work, we perform an in-depth study to achieve a comprehensive characterization of the microstructure evolution during FFF process of 316L SS. A direct fabrication approach enabling a controllable content of the second phase is developed without post-processing methods. First, the grain sizes and types of 316L SS sintered at 1573 K, 1613 K, and 1653 K are thoroughly quantified to unveil the microscopic morphology of the specimen at different sintering stages. This can help us understand the interlayer microstructure evolution process involving interlayer pores and dislocation density. Then, the phase composition and content of the specimen are analyzed using phase equilibrium simulation. The relationship between Cr element grain boundary segregation and δ-ferrite phase formation is established through phase characterization and element analysis. By combining the holding step of traditional solid solution treatment with sintering cooling process, we develop a new sintering temperature profile to enable the keep control of δ-ferrite phase content for the improvement of pitting corrosion resistance and mechanical properties of 316L SS parts. The findings in this work provide valuable insights into the complex meso-scale sintering behavior of FFF-fabricated meatal parts, paving a way for sintering process optimization in FFF of other metal alloys.

Table 1
FFF sintered metal parts characterized in the literature.

Material	Sintering conditions	Average grain size	Relative density	Literature
316L Stainless steel	1360 °C/ Vacuum	500 μm	> 95 %	[7]
	1380 °C/H_2	40.5 ± 6.9 μm	95.6 %	[9]
	1380 °C/H_2	45 μm	91–93 %	[10]
	1350 °C/Ar	40 μm	98.73 %	[11]
	1380 °C/H_2	50 ± 6 μm	98.5 %	[12]
	1320 °C HIP Sintering	-	99.7 %	[13]
	1380 °C/H_2	75 ± 20 μm	98.1 %	[14]
17–4 PH Stainless steel	1200 °C/Ar, H_2	6.5 μm	96.7 %	[15]
	1360 °C/H_2	-	95.6 %	[16]
	1360 °C/N_2	-	> 99.4 %	[17]
Cu	1030 °C/H_2	-	90.8 %	[6]
Inconel 718	1280 °C/ Vacuum	< 50 μm	> 97 %	[18]
Ti-6Al-4V	1340 °C/Ar	100 μm	91 %	[19]
W-Ni-Fe	1480 °C/Ar, H_2	37 μm	99.1 ± 0.2 %	[20,21]
W-Cu	1350 °C/H_2	< 2 μm	99.2 %	[22]

2. Methodologies

2.1. FFF process of 316L SS

The Ultrafuse 316L SS filament (BASF Corp., Ludwigshafen, Germany) used in this study consists of carbonyl iron powders and a polyoxymethylene-based binder system. Such high-purity ultrafine iron powders are spherical particles with a particle mean size of less than 10 μm, which can be used as the liquid phase during sintering to create nearly fully densified components [33]. 'Green' part printing step were produced with a desktop fused filament fabrication (FFF) printer (Lulzbot TAZ6, USA). The printing parameters are displayed in Table 2. The debinding step was conducted on a catalytic debinding system (CD3045, Elink Systems, USA) under 120 °C in a gaseous nitric acid

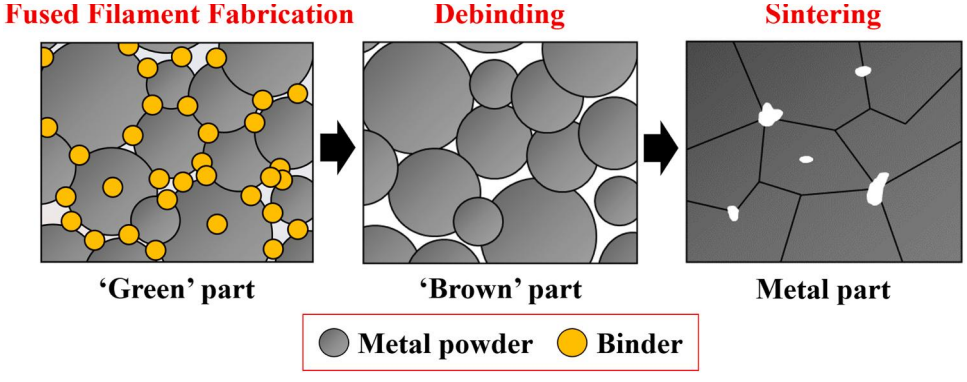

Fig. 1. Schematic diagram of metal FFF followed by debinding and sintering processes.

Table 2
Printing parameters for FFF process of 316L SS.

Printing parameters	Values
Nozzle temperature	240 °C
Nozzle size	0.5 mm
Infill density	100 %
Filling strategy	Alternating 45°
Printing speed	30 mm/s
Layer thickness	0.2 mm
Bed temperature	100 °C

atmosphere, which could remove approximately 97 wt% of the binder system. The debound 'brown' part was then transposed into a thermal furnace (MIM 3045, Elnik Systems, Cedar Grove, USA) under a pure hydrogen atmosphere. Based on Ning's previous work [34], the temperature evolution through the whole sintering process is shown in Fig. 2. Three sintering peak temperatures including 1573 K, 1613 K, and 1653 K were designed to reveal the microstructure of the specimens at different sintering temperatures for experimental characterization.

2.2. Microstructure characterization

The phase distribution, grain orientation mapping, and point scan analyses of 316L SS specimens after mechanical grinding and electropolishing were conducted using a scanning electron microscope (SEM, Nova NanoSEM 450, FEI Corp., USA) equipped with electron backscattered diffraction (EBSD) analyzer and energy dispersive spectroscopy (EDS). The EBSD analyzer has an acceleration voltage of 30 keV and a step size of 1 μm. EBSD data processing was conducted using TSL OIM analysis 7. The element content of the specimen sintered at 1653 K was analyzed by inductively coupled plasma optical emission spectrometry (ICP-OES) (Agilent 5800, Agilent Technologies). Carbon (C), oxygen (O), nitrogen (N), and sulfur (S) contents of the filament, debound 'brown' part, and specimens sintered at different temperatures were then measured using a high-frequency infrared carbon and sulfur (CS) analyzer (Corey-200, Deyang Kerui Instrument, China). The main phase structure characteristics of specimens were analyzed by X-ray diffraction (XRD) analyzer (Empyrean, Netherlands). The specimens sintered at 1653 K were prepared as a thin foil using focused ion beam (FIB) machining with gallium ion beam voltage of 30 kV and beam current dropping from 2 nA to 35 pA. During the FIB processing, the prepared lamella after cutting was a sheet of 10 μm × 10 μm with a thickness of 2 μm and continued to be reduced to below 100 nm with a gallium ion beam. High-resolution transmission electron microscopy (TEM, FEI talaos F200X, FEI, USA) was used to observe and calibrate the lattice orientation relationship between austenite grains and ferrite. The qualitative scanning analyses of element line distributions in grain-boundary-grain regions were performed using an electron probe micro-analyzer (EPMA) with a five-channel wavelength-dispersive spectrometer (JEOL JXA-8230, Japan). Average shrinkage after sintering was evaluated along the three different directions (X, Y, and Z (Building)) using a vernier caliper.

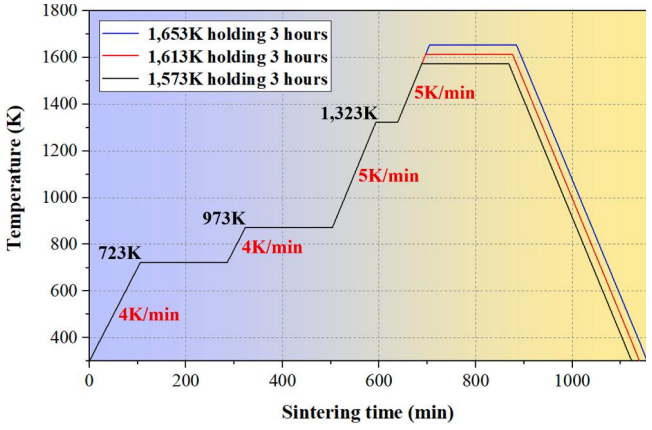

Fig. 2. Experimental sintering temperature profile.

2.3. Phase equilibrium simulation

Based on the assumption of thermodynamic equilibrium, the CALPHAD phase diagram was calculated for austenitic stainless steel using Thermo-Calc software (Version 2020b, Stockholm, Sweden). The phase composition, phase content, element content in each phase, and Gibbs free energy at equilibrium were evaluated using the TCFE9 steel/iron alloy database to gain insight into the phase transformation behavior of 316L SS at different sintering temperatures.

2.4. Corrosion testing

Corrosion measurements were accomplished with electrochemical workstation (CHI760, Wuhan, China). A three-electrode system was established using 316L SS specimen as a working electrode (WE), a platinum wire as a counter electrode (CE), and a saturated calomel electrode as a reference electrode (RE). Open circuit potential experiments of specimens sintered at 1653 K and modified heating process were carried out in aerated 3.5 % NaCl solution at 25 ℃ following the ASTM G61-86 [35]. After stabilization, electrochemical polarization measurements of all specimens were conducted with a scanning rate of 0.5 mV/s and a potential range between −400 mV and 1200 mV. The electrochemical impedance spectroscopy (EIS) measurements of all specimens were performed at frequencies ranging from 10^5 Hz to 10^{-2} Hz, with an excitation signal amplitude of 30 mV.

2.5. Mechanical property testing

Tensile tests of 316L SS specimens were performed on a universal testing system (MTS Systems Corporation, Eden Prairie, USA) with a loading capacity of 10 kN. The initial load was set to 100 N with the loading speed of 0.5 mm/min according to the ASTM E8 standard [36]. The detailed dimensions of the tensile specimens are depicted in Section 3.6.

3. Results and discussion

3.1. Microstructure evolution

For FFF process, layer-by-layer accumulation of powders during printing step is likely to cause an arranged distribution of metal particles in 'green' parts, leading to a certain directionality. Such directionality or particle rearrangement occurs in the early stage of sintering [24], which could be reflected in the final sintered part.

The grain orientation coloring diagram of the specimens along the building direction at three representative sintering temperatures are shown in Fig. 3. The specimens at each sintering temperature exhibit equiaxed austenite grains with a large number of annealing twinning structures. The cause of formation of austenite grains and twinning structure. Even with the presence of interlayer gaps left over from the printing step, the grain orientation is highly random. With the increase of sintering temperature, the grain size grows significantly. The average grain size at each sintering temperature is 17.82 μm (1573 K holding 3 h), 37.47 μm (1613 K holding 3 h), and 40.39 μm (1653 K holding 3 h), respectively. The grain size data at a densification temperature of 1653 K are consistent with previous literature reports [9,12]. It is obvious that the grain growth rate slows down with the increase of sintering temperature. The three directional average shrinkage of the specimens (Fig. 4) increase from 14 %~16 % at 1573 K to 16~18 % at 1653 K. For all sintering temperatures, the shrinkage of the specimen along the Z direction is about 1.5 % higher than that along the in-plane

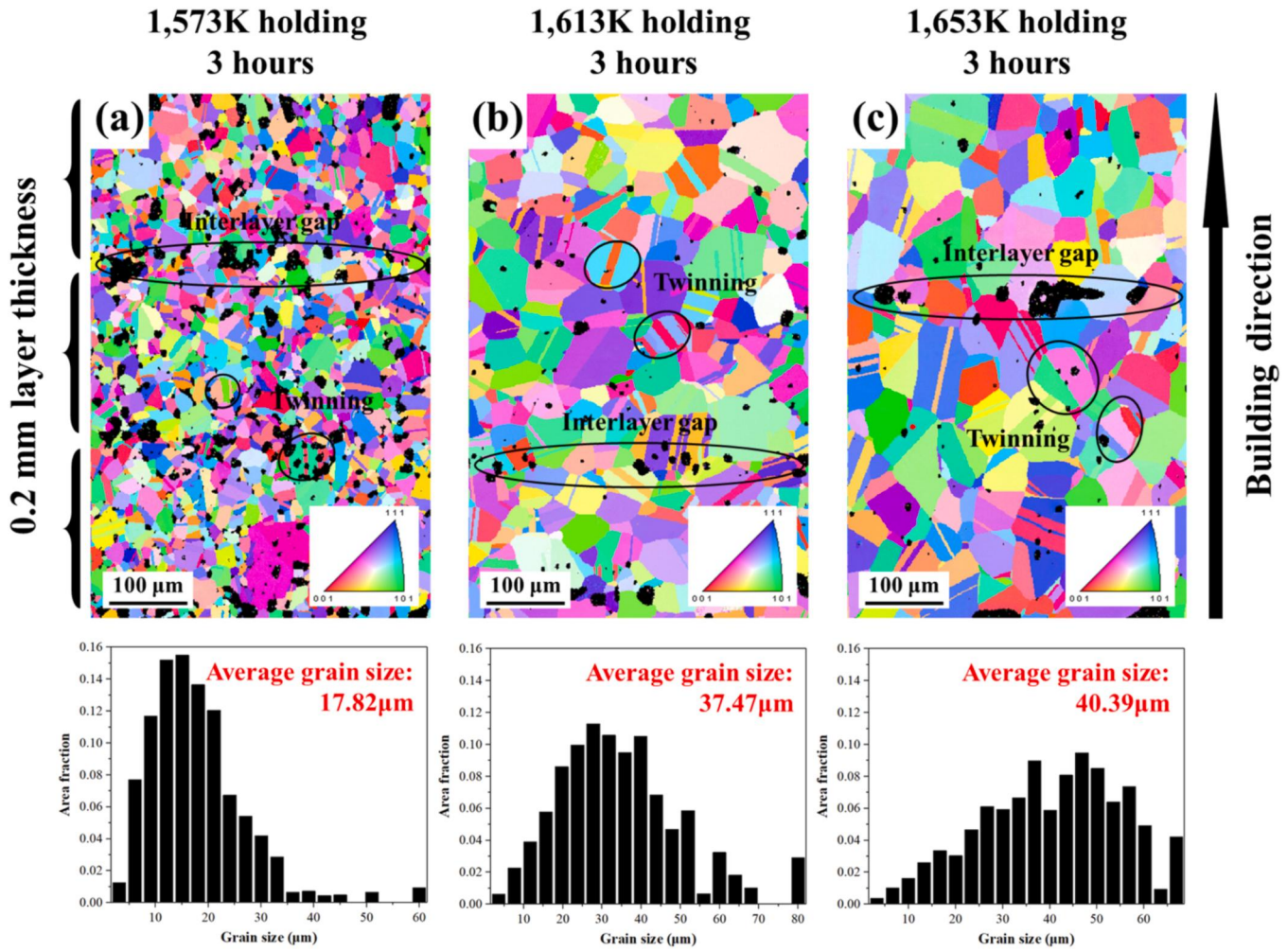

Fig. 3. EBSD analysis results along building direction: **(a)** 1573 K holding 3 h, **(b)** 1613 K holding 3 h, **(c)** 1653 K holding 3 h.

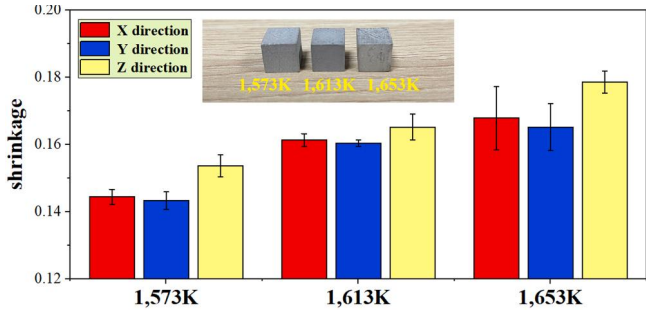

Fig. 4. Results of average size shrinkage for specimens at different sintering temperatures.

direction, showing anisotropic shrinkage.

The distributions of grain boundary orientation difference in the specimens at different sintering temperatures are shown in Fig. 5. All specimens represent a high relative frequency at 60° misorientation, with an area fraction of about 40 %, indicating a large amount of annealing twinning boundaries (TB). Furthermore, the orientation difference of the specimens is mainly distributed between 30° and 60°, indicating that the FFF-fabricated 316L SS part is dominated by high-angle grain boundaries (HAGB) [37]. When the orientation difference between adjacent grains is less than about 10°, it can be defined as a low-angle grain boundary (LAGB). As can be seen in Fig. 6(d), the area fraction of LAGB decreased from 11 % to 6.36 % with the increase of sintering temperature.

The HAGB/LAGB are mainly reflected in the hindering effect on dislocation slip. Due to the lower grain boundary energy, LAGB can accommodate more dislocations [38]. Therefore, dislocation movement is more likely to traverse the grain, and the local slip generated by which can enhance the dislocation density. During FFF process, the specimens at lower sintering temperature still retain large-sized interlayer pores after debinding along the building direction. At the same time, the shrinkage deformation along this direction leads to the formation of dislocation walls around the interlayer pores, and they further develop into LAGBs. Such structures at different sintering temperatures can be observed in the Kernel Average Misorientation (KAM) images, are shown in Fig. 6. The blue areas within austenite grains indicate low local orientation difference, while green, yellow, and red regions near interlayer pore regions (black) show larger local orientation differences. It is obvious that a large number of LAGBs are generated in the interlayer pore region when the sintering temperature reaches 1573 K. This can explain the higher shrinkage of the specimen along the building direction at the microscopic level.

With the increase in sintering temperature, the specimen continues to shrink and the thermal deformation behavior intensifies. At this time, the LAGBs will continue to absorb dislocations, with the continuous increase in internal storage energy. When the specimen shrinks to a certain extent, the austenite grains will undergo dynamic recrystallization. The LAGBs will gradually into stable HAGBs. Related studies have shown that a decrease in the number of LAGBs leads to the increase in

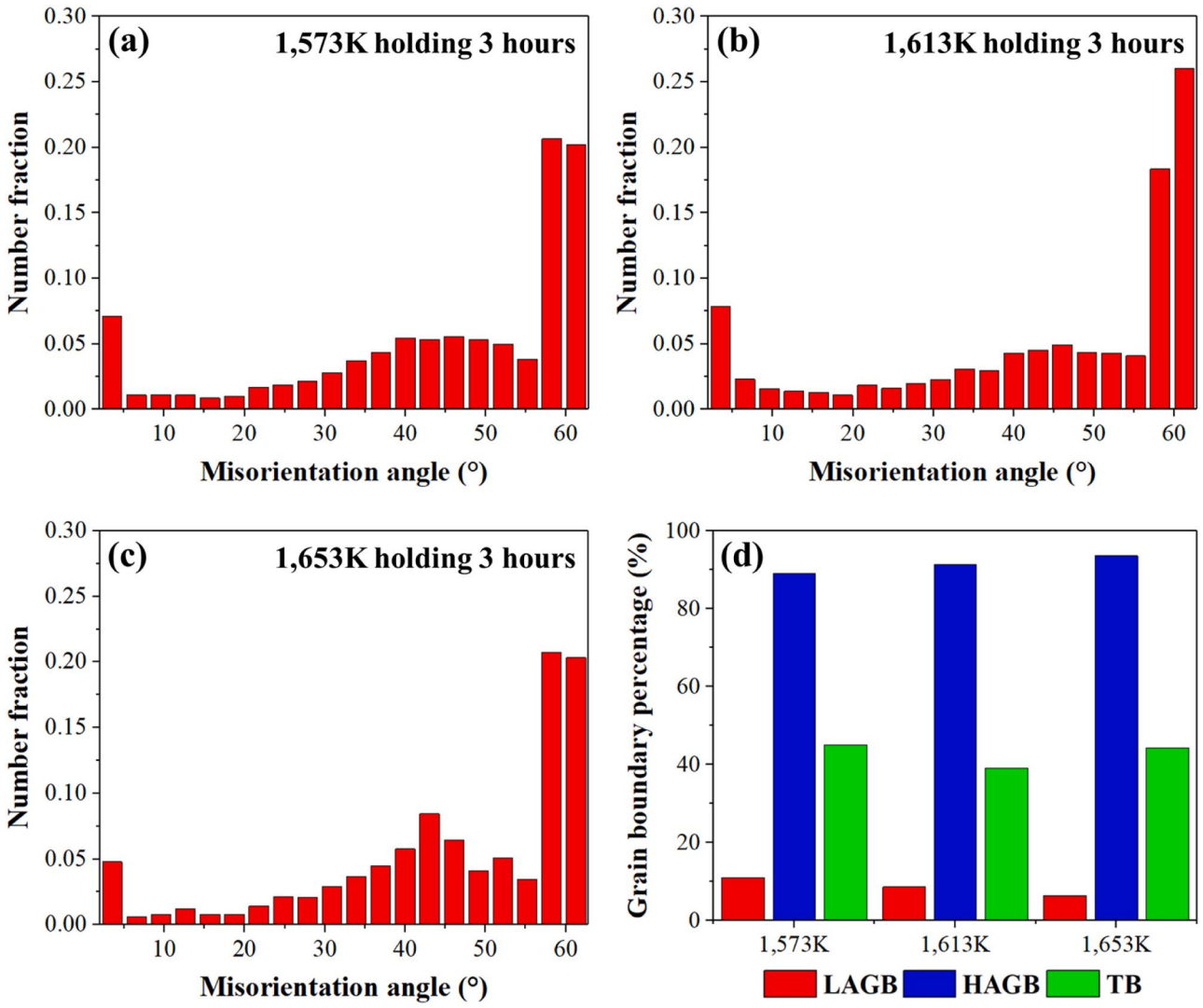

Fig. 5. Misorientation angle distribution: **(a)** 1573 K holding 3 h, **(b)** 1613 K holding 3 h, **(c)** 1653 K holding 3 h, **(d)** content statistics on different grain boundary types (LAGB: low-angle grain boundary, HAGB: high-angle grain boundary, and TB: twinning grain boundary).

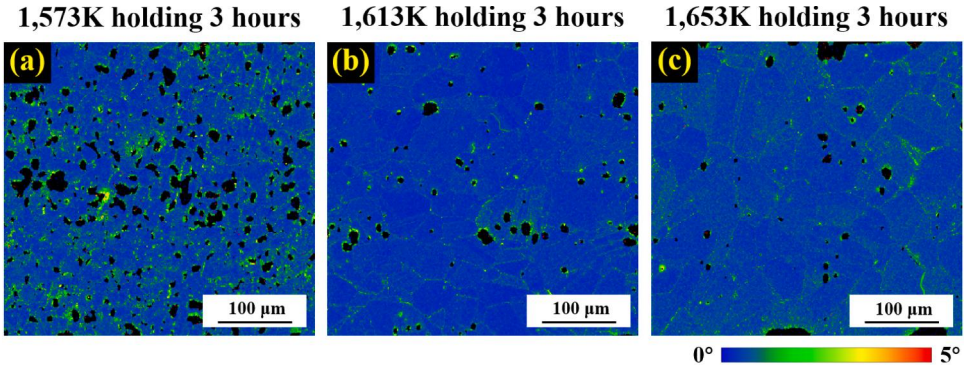

Fig. 6. Kernel Average Misorientation (KAM) images along building direction: **(a)** 1573 K holding 3 h, **(b)** 1613 K holding 3 h, **(c)** 1653 K holding 3 h.

the ductility of components [39]. However, the grain boundary energy of HAGBs is relatively high, and the dislocation movement needs to overcome and consume higher energy. Therefore, the formation of more HAGBs will create greater obstacles to dislocation slip, resulting in more dislocation disappearance. Finally, as the temperature reaches the densification temperature, further atomic diffusion and gradually disappearing pores will keep the specimen size constant. At this time, as the deformation resistance of austenite grains gradually disappears, the number of dislocations will stabilize.

The mean geometric dislocation density of specimens at different sintering temperatures can be quantified by KAM data. In this work, the local misorientation at a point (1 μm × 1 μm) is determined as follows according to surrounding points:

$$\Delta\theta_i = \frac{1}{n}\sum_{j=1}^{n}\left|\theta_{j,sur} - \theta_i\right| \quad (1)$$

where θ_i is the local misorientation of point i, $\theta_{j,sur}$ is the local misorientation at its neighboring point j. The mathematical relationship between geometrically necessary dislocation (GND) and local misorientation can be expressed by strain gradient theory:

$$\rho_{GND} = \frac{2\Delta\theta_i}{ub} = B\Delta\theta_i \quad (2)$$

where ρ_{GND} is the GND density of the region, u is the scanning step of EBSD (1 μm), and b is the buger vector. The mean GND density of specimens at different sintering temperatures can be calculated, as represented in Fig. 7. It is obvious that the average GND density is 16.866×10^{12} m^{-2} at 1573 K. When the sintering temperature reaches 1613 K, the mean GND density decreases to 13.586×10^{12} m^{-2} with the elimination of interlayer pores, and is basically consistent as that at 1653 K.

3.2. δ-ferrite phase formation

The ICP and CS analysis results of 316L SS sintered at 1653 K are shown in Table 3. The phase composition and content of 316L SS in thermodynamic equilibrium state are predicted in Fig. 8. The phase structure of the specimen mainly includes matrix phase and precipitation phase. The equilibrium phase fraction represents the formation of body-centered cubic (BCC) phase above 1540 K, which corresponds to δ-ferrite. Afterwards, the δ-ferrite phase fraction rapidly increases to 24.83 wt% with increasing equilibrium temperature from 1540 K to 1653 K. Phase content analysis shows that the sintered 316 L SS is comprised of γ-austenite and δ-ferrite phases. The self-diffusion coefficient of iron in BCC structure is much higher than that in more compact face-centered cubic (FCC) structure [40]. This might affect the final microstructure morphology of the FFF-fabricated metal parts.

For FFF process, precipitation of detrimental secondary phases caused by C enrichment must also be considered. The contents of non-metallic elements including C, O, N, and S of 316L SS specimens under different states are shown in Table 4. The initial C content in the filament is 2.434 wt%, and about 2 wt% is removed during the catalytic debinding process. In addition, it can be found that the highest C content exists at the sintering temperature of 1653 K. The increased C content has multiple effects on the stability of phases [41]. First, it can promote the super solidus liquid sintering process and the transformation from γ-austenite to δ-ferrite. Relevant reports have evidenced the important effect of the δ-ferrite phase on facilitating the part densification during sintering [42]. However, excess C content would lead to the formation of carbides ($M_{23}C_6$), specifically $Cr_{23}C_6$ in 316L SS. This may raise the potential risk of intergranular corrosion. Therefore, it is necessary to further analyze the phase composition.

However, an important disadvantage of excess C is the formation of carbides ($M_{23}C_6$), specifically $Cr_{23}C_6$ in 316L SS. This may raise the potential risk of intergranular corrosion. Therefore, it is necessary to further analyze the phase composition.However, an important disadvantage of excess C is the formation of carbides ($M_{23}C_6$), specifically with Cr. This may raise the potential risk of intergranular corrosion. Therefore, it is necessary to further analyze the phase composition.

The phase structures of the specimens at different sintering temperatures are quantified based on XRD, as shown in Fig. 9. It can be found that the specimens sintered at 1573 K consisted of γ-austenite only. Diffraction peaks are gradually formed along the (111) crystal plane in the specimen sintered at 1613 K, indicating a mixture of γ-austenite and a small amount of δ-ferrite. However, the peak value of the diffraction peak at the corresponding position in the specimen sintered at 1653 K increased slightly, indicating that the content of δ-ferrite gradually increased. Few carbides have been identified. The results of phase equilibrium simulation indicate that the equilibrium concentration of δ-ferrite in 316L SS at 1573 K is 5.66 wt%. Although moderate sintering cooling rate can promote the formation of δ-ferrite [41], the difference could be mainly caused due to the sintering dwell time involved in FFF process. For phase equilibrium simulations, the thermodynamic equilibrium state in a multiphase system is the limit state reached by the content variation of each phase [43], not involving any material transfer behavior at the macroscopic level. For FFF process, it could imply a longer holding time, allowing for the element interdiffusion between γ-austenite and δ-ferrite phases.

δ-ferrites fraction less than 5 wt% cannot be observed by XRD. Therefore, the phase distributions of the specimens sintered at different temperatures along the building direction are further characterized using EBSD objective analysis, as shown in Fig. 10. For the specimen sintered at 1573 K, a mixture of austenite grains (red) and pores (black) are obtained, corresponding to the XRD analysis results. The equiaxed/needle plate-like grains (green) distributed along the austenite grain boundaries in the specimens sintered at 1613 K and 1653 K are δ-ferrite grains. Related studies demonstrate that the presence of δ-ferrites with grid distribution is widely existed in this kind of 316L SS manufactured by the sintering-based metal AM process [44]. The quantitative statistical results in Fig. 10(d) demonstrate that the area fraction of δ-ferrite increases from 0.2 % at 1613 K to 1.4 % at 1653 K, indicating that the formation of δ-ferrite depends on the sintering temperature. On the other hand, the lower carbon content during low temperature sintering process could also affect the stability of δ-ferrite [45].

The nucleation sites of δ-ferrite are mostly distributed near the spherical pores inside the austenite grains, which could be closely related to the crystallographic orientation relationship between the two phases [46]. Further analysis shows that the crystallographic orientation relationship between the matrix phase and the precipitation phase is

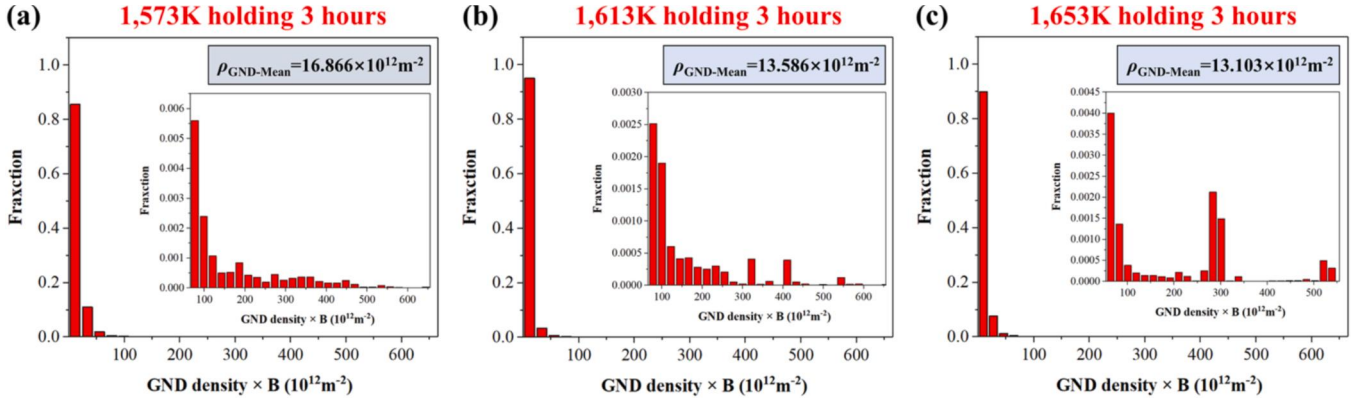

Fig. 7. Mean geometrically necessary dislocation (GND) density distribution: **(a)** 1573 K holding 3 h; **(b)** 1613 K holding 3 h; **(c)** 1653 K holding 3 h.

Table 3
Chemical elements of FFF-fabricated 316L SS (wt%).

Fe	Ni	Cr	C	Mo	Mn	Si	Cu	Co
Bal.	12.362	18.252	0.0228	1.985	1.082	0.453	0.250	0.107

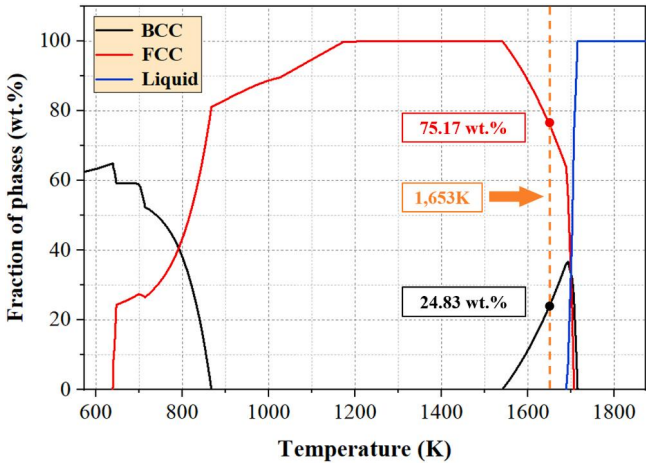

Fig. 8. Thermo-Calc equilibrium simulation results for FFF-fabricated 316L SS.

Table 4
Measured carbon, oxygen, nitrogen, and sulfur content of the filament, debound 'brown' part, and specimens sintered at different temperatures (wt%).

Specimen Status	Carbon	Oxygen	Nitrogen	Sulfur
Filament	2.434	60.06	0.251	0.00085
'Brown' part	0.515	0.203	0.146	0.00058
1573 K holding 3 h	0.0075	0.015	0.0015	0.0047
1613 K holding 3 h	0.0186	0.213	0.0019	0.0096
1653 K holding 3 h	0.0228	0.011	0.0018	0.0076

{111}< 1–10 >BCC//{110}< 1–11 >FCC (Kurdjumov-Sachs (KS) orientation [47,48]). This can be associated with the minimization of nucleation interface energy and activation barrier [46]. The Gibbs free energies of each phase at different temperatures are obtained, as shown in Fig. 12. It is concluded that the Gibbs free energy of each phase decreases with the increase of temperature, and the energy variation $\triangle G$ of BCC and FCC tends to 0 from 1613 K to 1653 K (blue area in Fig. 11), indicating a strong phase transition spontaneity. The above findings indicate that δ-ferrite is easier to form at high temperature stage, which indirectly reveals the microstructure formation and phase transition mechanisms of 316L SS during FFF-sintering process from the perspective of energy transfer/transformation.

TEM and fast fourier transform (FFT) selected area electron diffraction patterns are performed on the specimens sintered at 1653 K after FIB machining, as shown in Fig. 12. Fig. 12(a) to (c) represent high-resolution images of γ-austenite matrix and FFT diffraction spots. The interplanar spacing of the (111) plane is about 0.2 nm, and the corresponding crystal belt axis orientations are [112] and [011], respectively. Combined with the XRD results of the (111) plane in Fig. 9(a), it can be concluded that γ-austenite mainly grows mainly along a certain characteristic orientation in the (111) plane. The two-phase high-resolution image is shown in Fig. 12(d), in which the black line-shaded part is δ-ferrite. The results of FFT diffraction spot (Fig. 12(e)) illustrate that the δ-ferrite (111) plane coincides with the γ-austenite (111) plane, that is, (111) FCC//(111) BCC, indicating that the two-phase interface has a constrained coherent matching relationship. It is also found that δ-ferrite grows only along the (111) plane, which is consistent with Fig. 9(b).

3.3. Element content and distribution

The contents of the main elements in γ-austenite and δ-ferrite are calculated based on the phase equilibrium simulation, as shown in Table 5. It can be clearly seen that the content of Cr element in δ-ferrite is about 7 wt% higher than that of γ-austenite, while the content of Ni element is about 3 wt% lower.

Point scanning analysis is performed on specimens sintered at 1613 K and 1653 K to detect the nominal content of the main elements in austenite grains and δ-ferrites at the grain boundaries, as displayed in Fig. 13 and Table 6. It can be concluded that the Cr element content in δ-ferrites is about 25 wt%, while the content of Cr element in austenite grains is about 17 wt%. A content difference corresponds to the phase

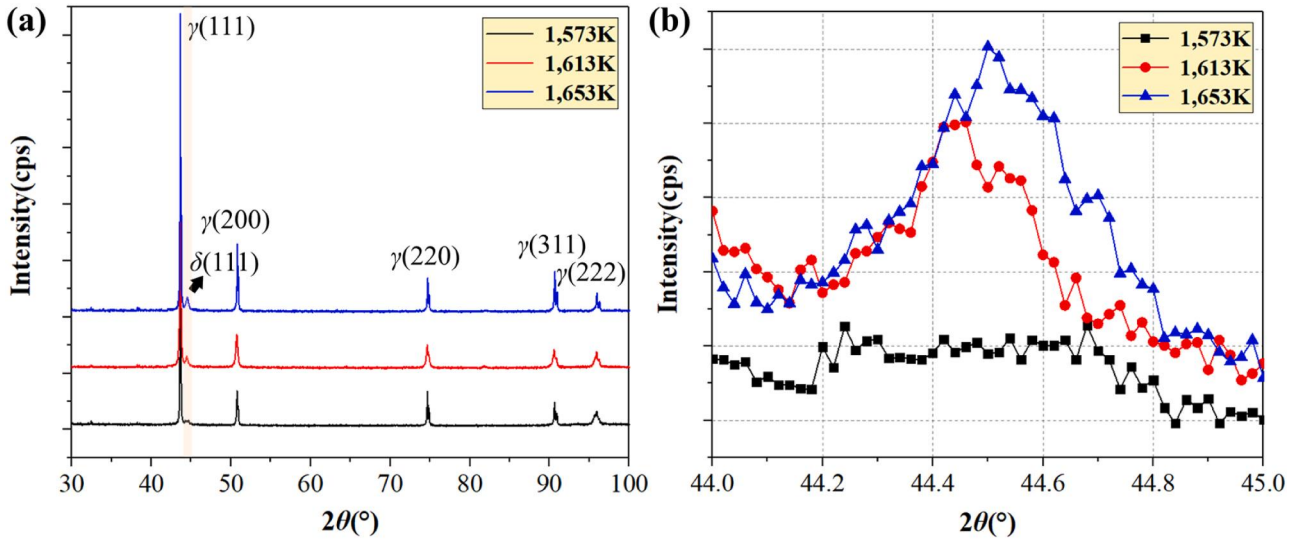

Fig. 9. (a) XRD spectra and **(b)** δ (111) peak magnification image (corresponding to the pink area in Fig. 10(a)) with different sintering temperatures (1573 K, 1613 K, and 1653 K).

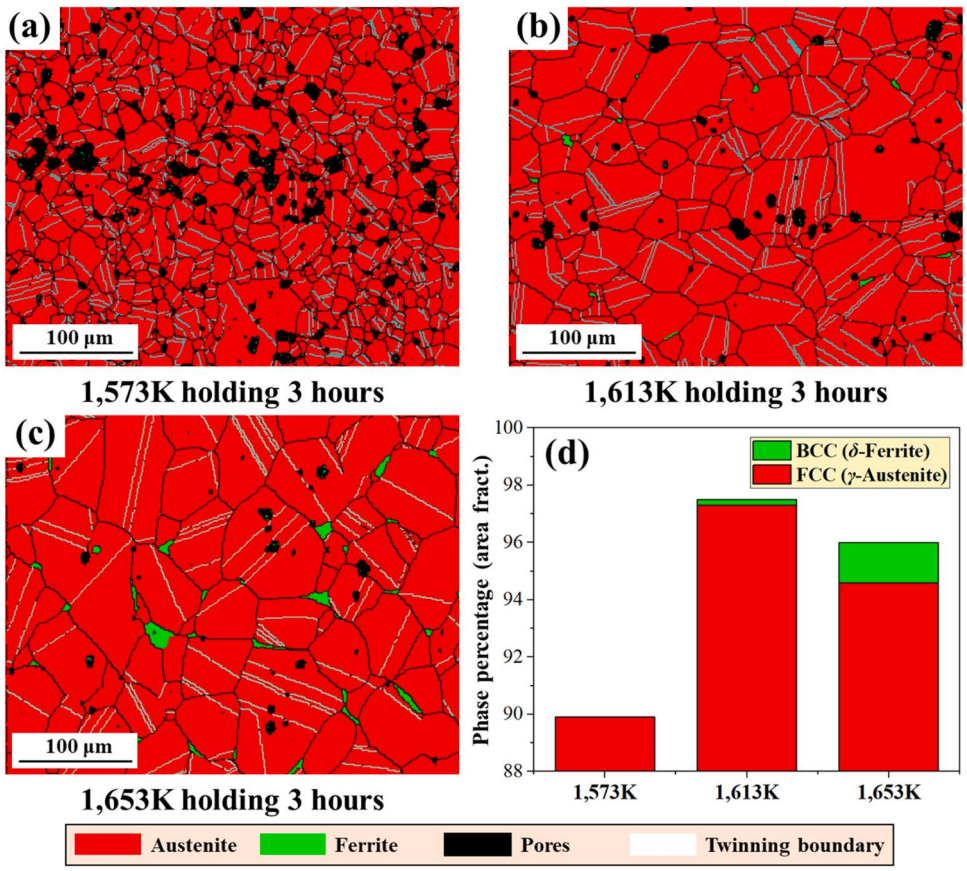

Fig. 10. EBSD Phase distribution along building direction: **(a)** 1573 K holding 3 h, **(b)** 1613 K holding 3 h, **(c)** 1653 K holding 3 h, **(d)** phase content statistics.

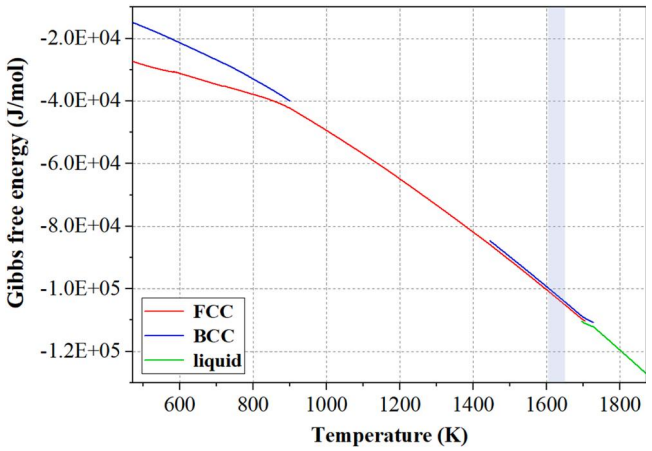

Fig. 11. Gibbs free energy of each phase.

equilibrium simulation results described above.

Further explore the macroscopic distribution of elements, EPMA is used to conduct qualitative scanning analysis on the element line distribution along the grain boundary region of the above specimens, as shown in Fig. 14. As the matrix element of 316L SS, Fe element has the highest concentration at each sintering temperature, while the intensity of Cr element in the grain boundary is significantly higher than that inside of the grain. However, both Fe and Ni elements at grain boundaries express lower intensity values (yellow areas in Fig. 14).

In most cases, Cr and Mo elements are usually defined as stabilizers of δ-ferrite, while Fe and Ni elements are regarded as stabilizers of γ-austenite [49]. Due to the excessive atomic diffusion at relatively high temperature holding stages, Cr atoms in austenite grains will move towards ferrites at grain boundaries. On the contrary, Fe/Ni atoms inside the ferrite grains will diffuse into the austenite grains. The vacancies formed by atomic diffusion in the two-phase grains will be replaced or filled by other atoms, resulting in a difference in element content, and maintains the constant number of total atoms in the system. This can also be demonstrated from Ning's mechanical work: vacancy formation/migration and solute element diffusion capacity [24]. On the other hand, further atomic diffusion and grain coarsening will result in the thickening of austenite grain boundaries [45]. This can accommodate more Cr atoms and promote their precipitation to the grain boundaries and eventually form stable grain boundaries anchored by a large number of δ-ferrites during the sintering holding and cooling stages. Therefore, the formation of δ-ferrite is strongly correlated to the Cr element grain boundary segregation.

3.4. Improvement of sintering profile

Related reports state that δ-ferrite is known to improve the ductility, toughness, and thermal cracking resistance of stainless steel [50,51]. However, excess δ-ferrites can also increase the potential risk of pitting corrosion [52–54]. For FFF process, it is important to control the content of δ-ferrite to prepare single-phase austenitic stainless steel with better corrosion resistance.

Solution treatment [55] is a heat treatment process in which an alloy is heated to a certain temperature and held for a period of time, finally cooled rapidly. For austenitic stainless steels, the holding temperature range is usually 1273 K to 1373 K [56], allowing the second phase to be fully dissolved into the austenitic matrix to obtain a single austenitic tissue. The austenitic transformation process is closely related to the holding temperature and time. A lower cooling rate could promote homogenous elemental distribution. For FFF process, the δ-ferrite content

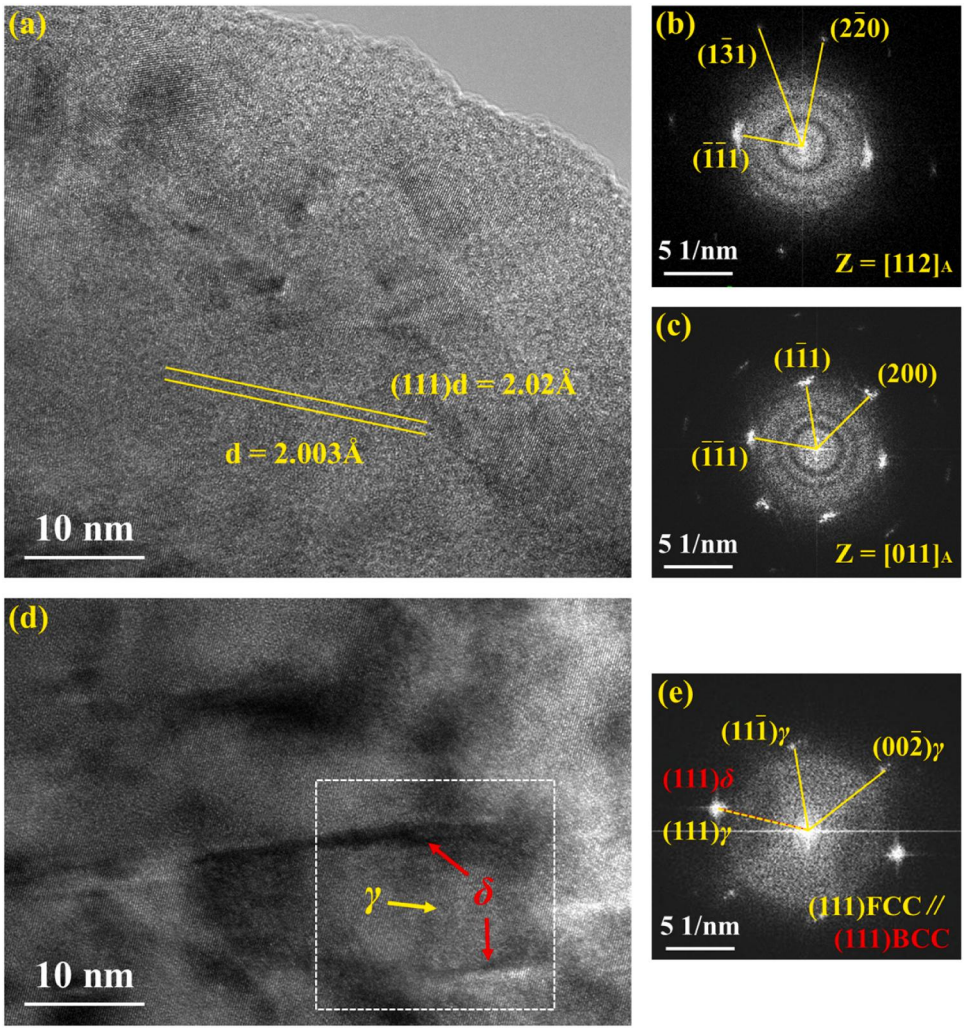

Fig. 12. High-resolution TEM images of specimens sintered at 1653 K: **(a)** γ-austenite lattice structure, **(b)** and **(c)** corresponding FFT diffraction spots, **(d)** two-phase interface lattice structure, **(e)** corresponding FFT diffraction spot.

Table 5
Thermo-Calc equilibrium simulation results of element content in different phases.

Temperature	Phase	Element content (wt%)				
		Fe	Ni	Cr	Mo	Mn
1613 K	γ-austenite	69.32	10.88	15.81	1.73	1.12
	δ-ferrite	68.53	7.70	19.13	2.79	0.87
1653 K	γ-austenite	69.29	11.31	15.48	1.60	1.15
	δ-ferrite	68.78	8.22	18.50	2.61	0.91

can be controlled by adding the holding step of solution treatment during the sintering cooling process, to obtain single-phase austenitic 316L SS. Specifically, an additional 1373 K holding for 1 h during the sintering cooling stage with a cooling rate of 5 K/min was applied in a modified process, as shown in Fig. 15.

The element distribution of the specimen fabricated by the modified sintering process is displayed in Fig. 16. It is obvious that each element is uniformly distributed, without segregation phenomenon. The microstructure morphology of the specimen is characterized in Fig. 17. Compared with original sintering processes (3 h holding at 1653 K) in Fig. 2, more equiaxed austenite grains can be observed. The average grain size of the specimen has grown from 40.39 μm to 68.42 μm (Fig. 17(d)). This behavior could be associated with the further grain boundary migration caused by additional holding process. From KAM data calculation, the mean GND density (Fig. 17(e)) of the specimen has also increased from 13.103×10^{12} m^{-2} to 18.186×10^{12} m^{-2}. In addition, it can be seen that the δ-ferrites precipitated along the grain boundaries have been eliminated from EBSD analysis results in Fig. 17 (c). The XRD result in Fig. 17(f) also shows that the diffraction peak formed along the (111) crystal plane has disappeared. Obviously, single-phase austenitic 316L SS has been successfully prepared.

3.5. Corrosion properties

The elimination of solute element segregation and second phase precipitation will have a strong impact on the corrosion resistance of metal components [57]. This section evaluates the pitting corrosion resistance of 316L SS fabricated by two sintering heating processes (original and modified), respectively.

The results of the polarization curves of 316L SS specimens fabricated by two sintering processes are shown in Fig. 18. Tafel fitting is applied to analyze corrosion potential (E_{corr}), corrosion current density (i_{corr}), and breakdown potential (E_b), as displayed in Table 7. The modified process built specimen exhibits the lowest i_{corr} value (0.18 μA/cm^2), indicating a slower electron loss rate. The E_{corr} values and polarization curves for the two specimens reveal that the pitting potential for modified process (−342 mV) is considerably higher than that for unmodified process (−512 mV), indicating improved corrosion performance after the application of 1 h holding during sintering cooling.

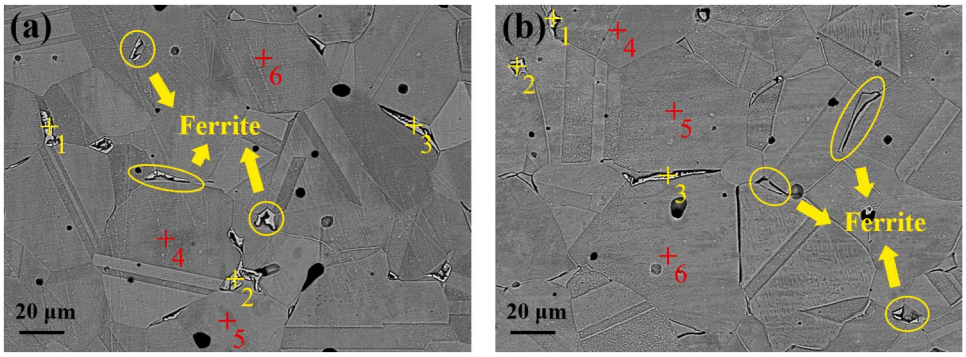

Fig. 13. High magnification SEM images of 316L SS specimens at different sintering temperatures: **(a)** 1613 K holding 3 h, **(b)** 1653 K holding 3 h.

Table 6
EDS dot mapping results.

Specimen	Phase	Scanning area	Element content (wt%)				
			Fe	Ni	Cr	Mo	Mn
1613 K holding 3 h	δ-ferrite	Point 1	64.49	3.42	25.46	3.86	0.93
	δ-ferrite	Point 2	63.25	4.62	25.66	3.85	0.95
	δ-ferrite	Point 3	59.15	3.70	28.99	5.31	0.60
	γ-austenite	Point 4	68.39	10.12	17.35	1.65	0.92
	γ-austenite	Point 5	68.07	9.85	17.56	1.87	1.04
	γ-austenite	Point 6	68.51	9.89	17.24	1.80	1.01
1653 K holding 3 h	δ-ferrite	Point 1	57.07	3.37	27.86	6.24	0.92
	δ-ferrite	Point 2	66.45	4.96	25.18	1.83	1.14
	δ-ferrite	Point 3	53.34	3.33	24.72	7.27	0.79
	γ-austenite	Point 4	66.55	9.99	16.14	1.88	0.72
	γ-austenite	Point 5	69.40	9.03	18.17	0.96	1.28
	γ-austenite	Point 6	65.43	10.52	15.90	1.95	1.10

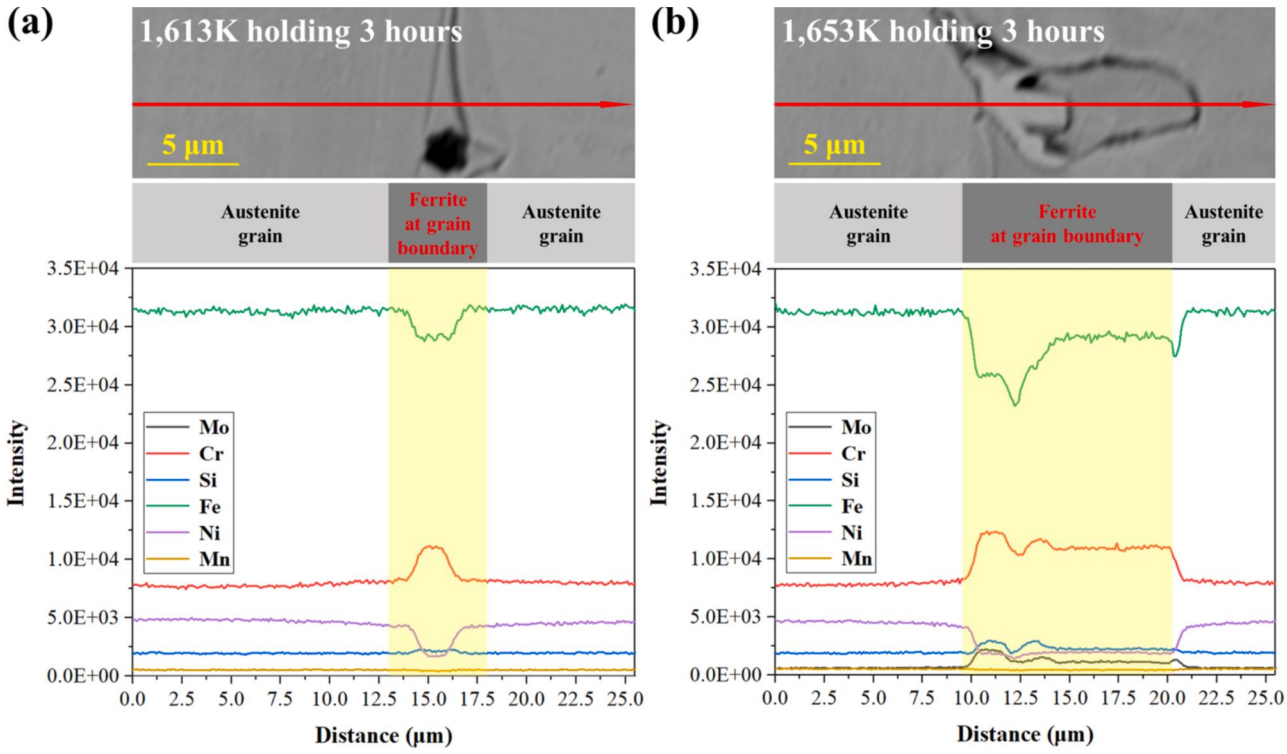

Fig. 14. EPMA line-scanning results of 316L SS specimens at different sintering temperatures: **(a)** 1613 K holding 3 h, **(b)** 1653 K holding 3 h.

Chao et al. [58] reported that the reduction in the pitting potential of 316L SS could be attributed to the elimination of residual stress during heat treatment. In addition, it has been found that surface defects such as pores and surface roughness can also have a ngative impact on the pitting corrosion resistance of 316L SS [59]. For FFF process, high porosity levels caused by inherent interlayer defects could affect the

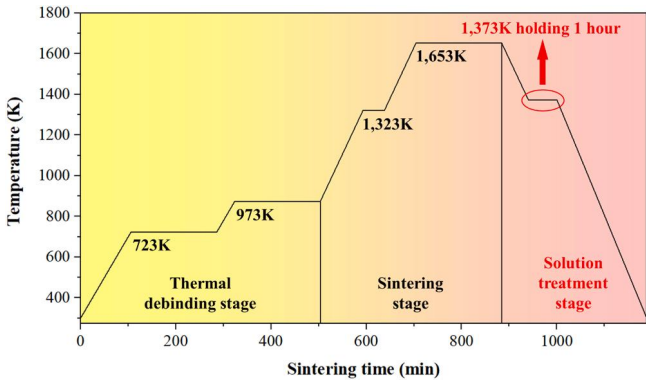

Fig. 15. Modified sintering curve based on solution treatment, by adding 1373 K holding 1 h during cooling stage.

pitting corrosion resistance of the matrix (see Fig. 3). More importantly, the single-phase austenitic eliminates the potential effects of the brittle phase formation in Cr-enriched regions on pitting corrosion resistance.

Fig. 19 shows the electrochemical impedance spectroscopies of the two specimens, which Nyquist plots can be fitted by Randle equivalent circuit diagram. In this circuit, R_S is solution resistance, CPE is double layer capacitance, and R_{CT} is charge transfer resistance, respectively. The fitting parameters are displayed in Table 8. The Nyquist plots indicate that the diameter of the modified-process built specimen is larger than that of unmodified-process built specimen. A higher R_{CT} value reflects a thicker passivation layer, which improves the corrosion resistance of the specimen [60]. Relevant studies show that there is a significant correlation between R_{CT} value and pore defects [61]. The solution treatment applied during the sintering cooling process allows for further atomic diffusion, which will help to further eliminate pores and then improve corrosion resistance. Conversely, the relatively low R_{CT} value indicates the enhanced ability of chloride ions to pass through CPE, which accelerates the breakdown of the passivation layer. The above results confirm that the modified-process built specimen has better pitting corrosion resistance.

3.6. Tensile properties

Engineering stress–strain curves of 316L SS specimens fabricated by two sintering processes under tensile tests are shown in Fig. 20. They exhibit similar trends of elongation at fracture between 80 % and 90 %, meeting the UNS S31603 standard requirements [62]. The specimen fabricated by the modified sintering process can yield a higher tensile strength (about 20 % higher than the original sintering process) under the condition of additional grain growth. This difference could be explained by the "solid solution strengthening" effect during the additional holding process that dissolves δ-ferrite phase into the matrix. As shown in Fig. 17(e), the atomic displacement of the δ-ferrite phase during the dissolution could lead to the redistribution of dislocation movement, thereby increasing the dislocation density. Eventually, the high energy dislocation network enhances the ability of dislocation pinning, resulting in work hardening and improved material strength.

4. Conclusions and future research

In this work, the microstructure morphology and orientation, phase structure, and element distribution of 316L SS during FFF process were systematically characterized. The relationship between Cr segregation at grain boundaries and δ-ferrite formation was established. Subsequently, an improved sintering process was developed to control the precipitation of δ-ferrite, and the modified process can significantly improve the pitting corrosion resistance of 316L SS. The findings in this work resulted in the following conclusions:

(1) All specimens exhibited equiaxed austenite grains with average equivalent grain sizes of 17.82 μm, 37.47 μm, and 40.39 μm, respectively. The specimens at 1573 K displayed a weaker grain orientation. When the sintering temperature rose to 1653 K, the randomness of grain orientation in specimens gradually increased, with the texture strength decreasing from 2.561 to 2.122.

(2) The area fraction of LAGBs in EBSD results at 1573 K was 11 %, which dropped to 6.36 % at 1653 K. The low dislocation density caused by the lack of interlayer pores can be considered as the fundamental reason for the decrease of the number of LAGBs under high temperature sintering conditions.

(3) The specimens were transformed from a γ-austenitic phase at 1573 K to a mixture of austenite and δ-ferrite phase at 1613 K. Finally, the area fraction of δ-ferrite phase in EBSD results increased from 0.2 % to 1.4 % at 1653 K, showing a typical KS orientation relationship and a coherent interface relationship.

(4) The Cr element was defined as a fixed element δ-ferrite that promoted its formation. Phase equilibrium simulation results showed that the content of Cr element in δ-ferrite is about 7 wt% higher than that of γ-austenite, which is highly consistent with EDS point scanning results.

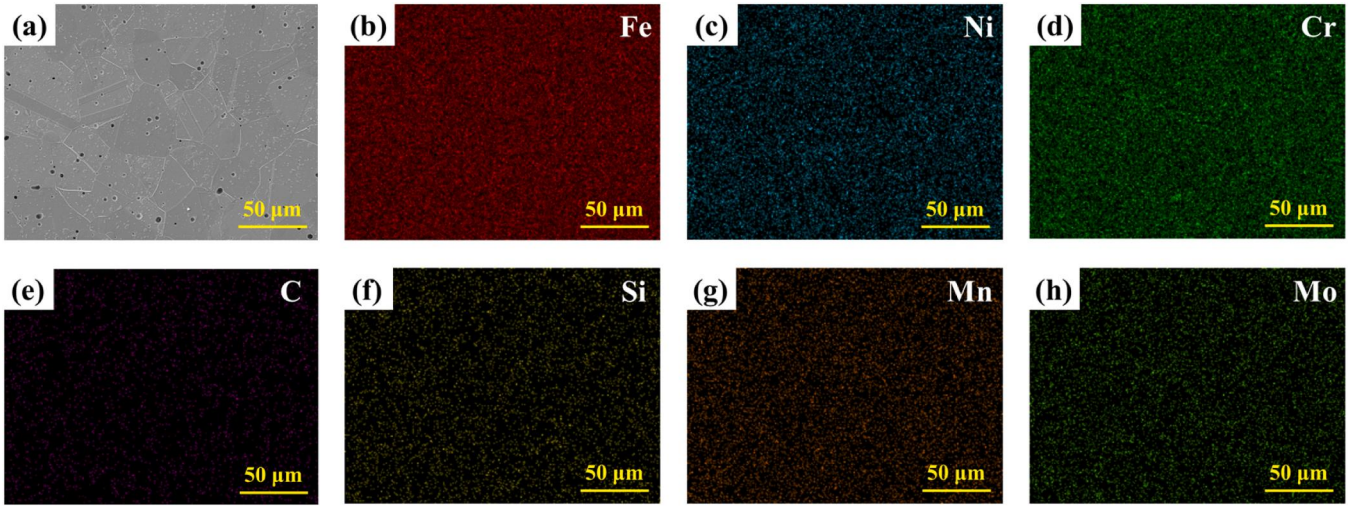

Fig. 16. High magnification SEM image and dot mapping for element distribution in 316L SS fabricated by the modified sintering process.

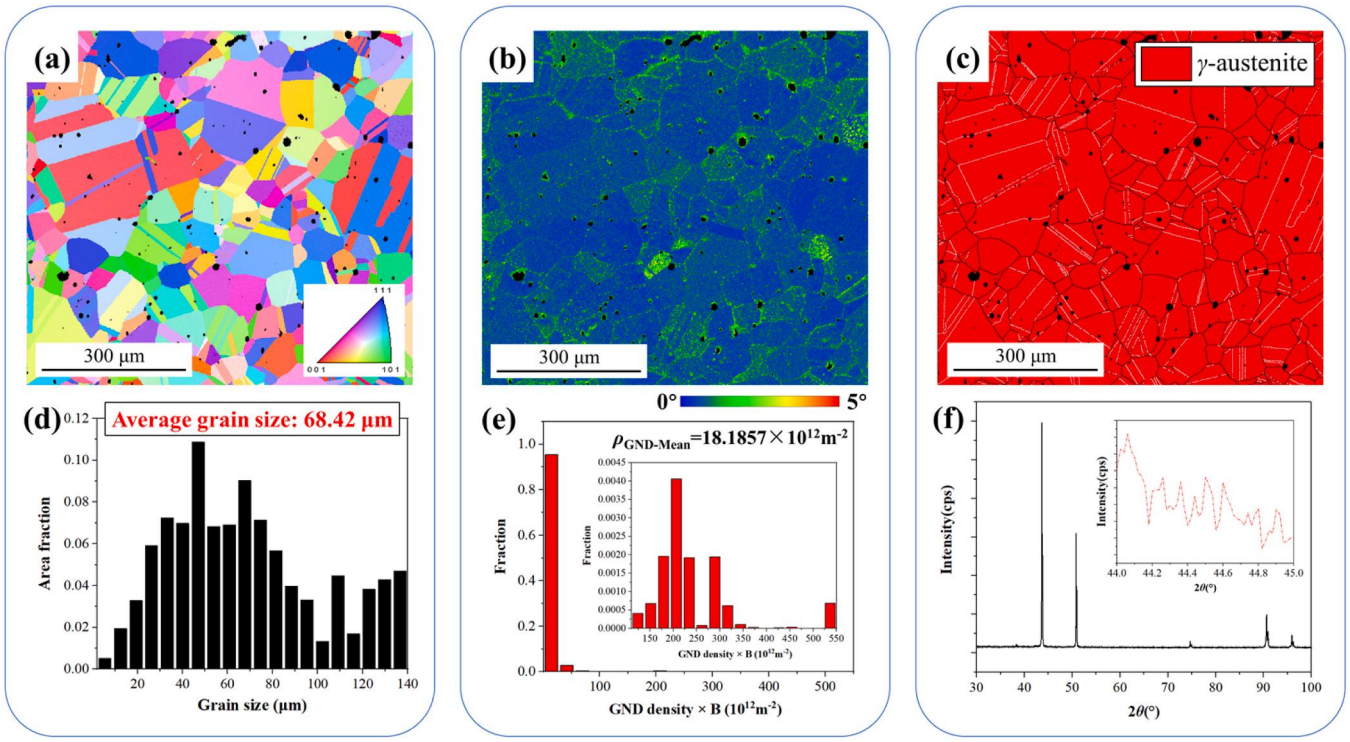

Fig. 17. Microstructure of 316L SS specimen fabricated by modified sintering process: **(a)** grain orientation, **(b)** KAM image, **(c)** phase distribution, **(d)** grain size distribution, **(e)** GND distribution, **(f)** XRD spectra.

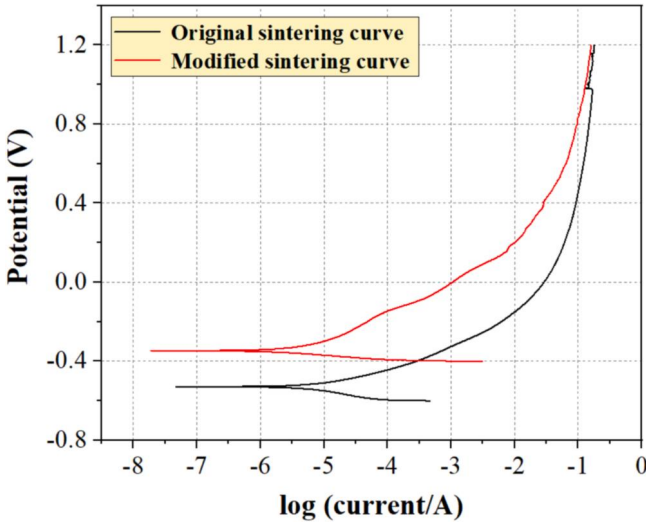

Fig. 18. Electrochemical polarization curves of 316L SS specimens.

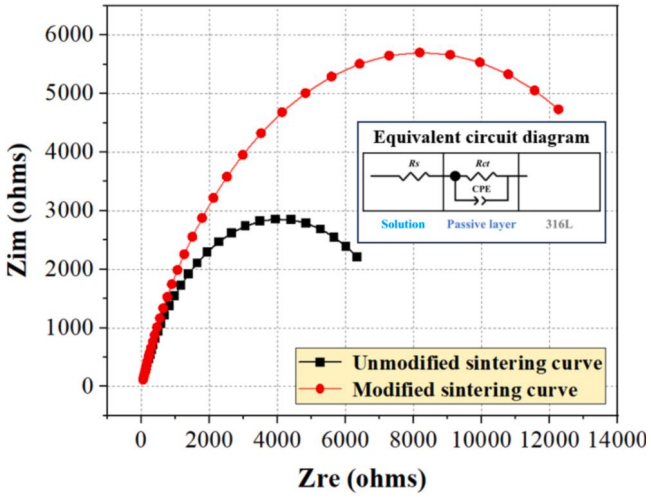

Fig. 19. Electrochemical impedance spectroscopies of 316L SS specimens.

Table 7
Tafel fitting parameters.

Specimen	E_{corr} (mV)	I_{corr} (μA/cm^2)	E_b (mV)
Original (3 h holding at 1653 K)	-512	1.5	-100
Modified	-342	0.18	34

Table 8
Fitting parameters obtained from electrochemical impedance spectroscopy plots.

Specimen	R_S (Ω·cm^2)	R_{CT} (Ω·cm^2)	Q (S·sec^n·cm^{-2})
Original (3 h holding at 1653 K)	7.01	1.43E4	9.63E-5
Modified	6.56	1.45E5	7.116E-5

(5) Specimen with single-phase austenite can be obtained by adding 1 h constant temperature at 1373 K during the sintering cooling process. The results of electrochemical measurements show that the pitting corrosion resistance and the of the specimen is improved compared to the original sintering process. The tensile test results suggest that the tensile strength of the specimen is 579 MPa, increasing by 20 %.

The modified process in this study can offer a new idea for controlling phase content to optimize the final microstructure of metal components. Future studies would be targeted at optimizing cooling

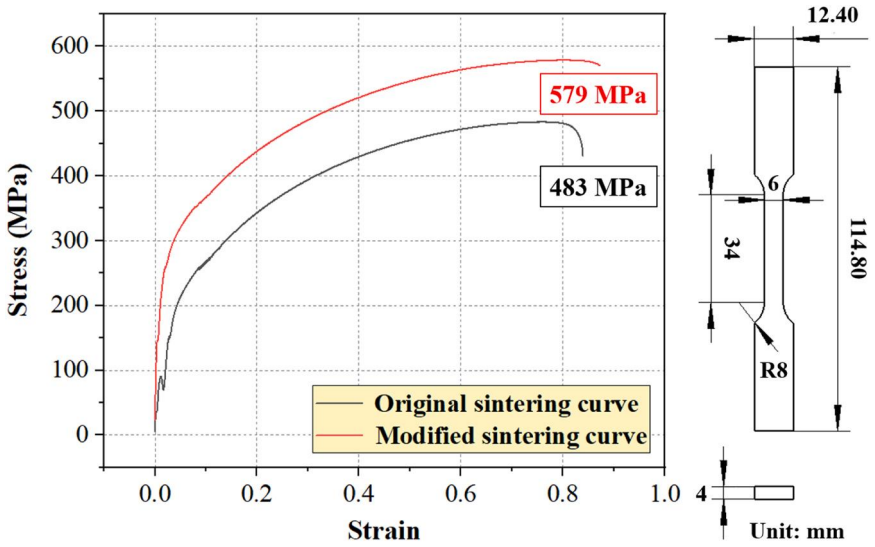

Fig. 20. Engineering stress–strain curves of 316 L SS specimens.

temperature, cooling rate, and holding time to create 316L SS components with stronger pitting corrosion resistance and mechanical properties.

CRediT authorship contribution statement

Fuji Wang: Resources, Funding acquisition, Supervision. **Siyao You:** Conceptualization, Methodology, Software, Data curation, Visualization, Writing – original draft. **Dayue Jiang:** Conceptualization, Methodology, Validation, Investigation, Writing – review & editing. **Xiangyu Yuan:** Methodology, Data curation. **Rao Fu:** Methodology, Supervision. **Fuda Ning:** Conceptualization, Methodology, Funding acquisition, Project administration, Writing – review & editing, Supervision.

Declaration of Competing Interest

The authors declare that they have no known competing financial interests or personal relationships that could have appeared to influence the work reported in this paper.

Acknowledgments

Fuda Ning would like to acknowledge the support from the U.S. National Science Foundation through award (CMMI-2224309) as well as the grant (#ADLG241) from Small Scale Systems Integration and Packaging (S^3IP) Center of Excellence, funded by New York Empire State Development's Division of Science, Technology and Innovation. Fuji Wang appreciates the support from Liaoning Revitalization Talents Program (Grant No. XLYC1801008, XLYCYSZX1901, and XLYC1902014), Science and Technology Innovation Foundation of Dalian (Grant No. 2019CT01).

References

[1] P. Kumar, R. Jayaraj, J. Suryawanshi, U.R. Satwik, J. Mckinnell, U. Ramamurty, Fatigue strength of additively manufactured 316L austenitic stainless steel, Acta Mater. 199 (2020) 225–239, https://doi.org/10.1016/j.actamat.2020.08.033.
[2] K.M. Bertsch, G.M. de Bellefon, B. Kuehl, D.J. Thoma, Origin of dislocation structures in an additively manufactured austenitic stainless steel 316L, Acta Mater. 199 (2020) 19–33, https://doi.org/10.1016/j.actamat.2020.07.063.
[3] C. Gao, S. Wolff, S. Wang, Eco-friendly additive manufacturing of metals: energy efficiency and life cycle analysis, J. Manuf. Syst. 60 (2021) 459–472, https://doi.org/10.1016/j.jmsy.2021.06.011.
[4] A.C. Rios, E. Olevsky, E. Hryha, M. Persson, R.K. Bordia, Analytical models for initial and intermediate stages of sintering of additively manufactured stainless steel, Acta Mater. 249 (2023), 118822, https://doi.org/10.1016/j.actamat.2023.118822.
[5] A. Bose, C.A. Schuh, J.C. Tobia, N. Tuncer, N.M. Mykulowycz, A. Preston, A. C. Barbati, B. Kernan, M.A. Gibson, D. Krause, T. Brzezinski, J. Schroers, R. Fulop, J.S. Myerberg, M. Sowerbutts, Y.M. Chiang, A. John Hart, E.M. Sachs, E.E. Lomeli, A.C. Lund, Traditional and additive manufacturing of a new Tungsten heavy alloy alternative, Int. J. Refract. Met. Hard Mater. 73 (2018) 22–28, https://doi.org/10.1016/j.ijrmhm.2018.01.019.
[6] G. Singh, J. Missiaen, D. Bouvard, J. Chaix, Copper extrusion 3D printing using metal injection moulding feedstock: analysis of process parameters for green density and surface roughness optimization, Addit. Manuf. 38 (2021), 101778, https://doi.org/10.1016/j.addma.2020.101778.
[7] Y. Thompson, J. Gonzalez-Gutierrez, C. Kukla, P. Felfer, Fused filament fabrication, debinding and sintering as a low cost additive manufacturing method of 316L stainless steel, Addit. Manuf. 30 (2019), 100861, https://doi.org/10.1016/j.addma.2019.100861.
[8] E.A. Olevsky, Theory of sintering: from discrete to continuum, Mater. Sci. Eng. R. Rep. 23 (1998) 41–100, https://doi.org/10.1016/S0927-796X(98)00009-6.
[9] D. Jiang, F. Ning, Additive manufacturing of 316L stainless steel by a printing-debinding-sintering method: effects of microstructure on fatigue property, J. Manuf. Sci. E-T. ASME 143 (2021), 091007, https://doi.org/10.1115/1.4050190.
[10] M. Sadaf, M. Bragaglia, F. Nanni, A simple route for additive manufacturing of 316L stainless steel via Fused Filament Fabrication, J. Manuf. Process. 67 (2021) 141–150, https://doi.org/10.1016/j.jmapro.2021.04.055.
[11] R. Santamaria, M. Salasi, S. Bakhtiari, G. Leadbeater, M. Iannuzzi, M.Z. Quadir, Microstructure and mechanical behaviour of 316L stainless steel produced using sinter-based extrusion additive manufacturing, J. Mater. Sci. 57 (2022) 9646–9662, https://doi.org/10.1007/s10853-021-06828-8.
[12] J. Damon, S. Dietrich, S. Gorantla, U. Popp, B. Okolo, V. Schulze, Process porosity and mechanical performance of fused filament fabricated 316L stainless steel. Rapid Prototyp. J. 25 (2019) 1319–1327, https://doi.org/10.1108/RPJ-01-2019-0002.
[13] Y. Wang, L. Zhang, X. Li, Z. Yan, On hot isostatic pressing sintering of fused filament fabricated 316L stainless steel-Evaluation of microstructure, porosity, and tensile properties, Mater. Lett. 296 (2021), 129854, https://doi.org/10.1016/j.matlet.2021.129854.
[14] M.A. Wagnera, J. Engela, A. Hadianb, F. Clemensb, M. Rodriguez-Arbaizarc, E. Carreño-Morellic, J.M. Wheelera, R. Spolenak, Additive manufacturing of 316L stainless-steel structures using fused filament fabrication technology: mechanical and geometric properties, Rapid Prototyp. J. 27 (2021) 583–591, https://doi.org/10.1108/RPJ-06-2020-0120.
[15] T.C. Henry, M.A. Morales, D.P. Cole1, C.M. Shumeyko, J.C. Riddick, Mechanical behavior of 17-4 PH stainless steel processed by atomic diffusion additive manufacturing, J. Adv. Manuf. Technol. 114 (2021) 2103–2114, https://doi.org/10.1007/s00170-021-06785-1.
[16] G. Singh, J.M. Missiaen, D. Bouvard, J.M. Chaix, Additive manufacturing of 17-4 PH steel using metal injection molding feedstock: analysis of 3D extrusion printing, debinding and sintering, Addit. Manuf. 41 (2021), 102287, https://doi.org/10.1016/j.addma.2021.102287.
[17] Y. Zhang, AljoschaRoch, Fused filament fabrication and sintering of 17-4 PH stainless steel, Manuf. Lett. 33 (2022) 29–32, https://doi.org/10.1016/j.mfglet.2022.06.004.
[18] Y. Thompson, K. Zissel, A. Förner, J. Gonzalez-Gutierrez, C. Kukla, S. Neumeier, P. Felfer, Metal fused filament fabrication of the nickel-base superalloy IN 718, J. Mater. Sci. 57 (2022) 9541–9555, https://doi.org/10.1007/s10853-022-06937-y.

[19] Y. Zhang, S. Bai, M. Riede, E. Garratt, A. Roch, A comprehensive study on Fused Filament Fabrication of Ti-6Al-4V structures, Addit. Manuf. 34 (2020), 101256, https://doi.org/10.1016/j.addma.2020.101256.

[20] Z. Hu, Y. Liu, Z. Qian, Y. Zhao, J. Dong, Z. Yang, Z. Wang, Z. Ma, The preparation of high-performance 96W-2.7Ni-1.3Fe alloy parts by powder extrusion 3D printing, Mater. Sci. Eng. A. 817 (2021), 141417, https://doi.org/10.1016/j.msea.2021.141417.

[21] A. Bose, J.P. Reidy, N. Tuncer, L. Jorgensen, Processing of tungsten heavy alloy by extrusion-based additive manufacturing, Int. J. Refract. Met. Hard Mater. 110 (2023), 106021, https://doi.org/10.1016/j.ijrmhm.2022.106021.

[22] L. Zhuo, C. Liu, E. Yin, Z. Zhao, S. Pang, Low-cost and low-temperature 3D printing for refractory composite inspired by fused deposition modeling and binder jetting, Compos. Part A Appl. Sci. Manuf. 162 (2022), 107147, https://doi.org/10.1016/j.compositesa.2022.107147.

[23] T. Kurose, Y. Abe, M.V.A. Santos, Y. Kanaya, A. Ishigami, S. Tanaka, H. Ito, Influence of the layer directions on the properties of 316L stainless steel parts fabricated through fused deposition of metals, Mater 13 (2020) 2493, https://doi.org/10.3390/ma13112493.

[24] F. Wang, S. You, D. Jing, F. Ning, Study on sintering mechanism for extrusion-based additive manufacturing of stainless steel through molecular dynamics simulation, Addit. Manuf. 58 (2022), 102991, https://doi.org/10.1016/j.addma.2022.102991.

[25] M.A. Wagner, J. Engel, A. Hadian, F. Clemens, M. Rodriguez-Arbaizar, E. Carreño-Morelli, J.M. Wheeler, R. Spolenak, Filament extrusion-based additive manufacturing of 316L stainless steel: effects of sintering conditions on the microstructure and mechanical properties, Addit. Manuf. 59 (2022), 103147, https://doi.org/10.1016/j.addma.2022.103147.

[26] S. Kim, H. Kwon, H. Kim, Effect of delta ferrite on corrosion resistance of type 316L stainless steel in acidic chloride solution by micro-droplet cell, Solid. State Phenom. 124–126 (2007) 1533–1536, https://doi.org/10.4028/www.scientific.net/SSP.124-126.1533.

[27] F.C. Pinto, I.R. Souza Filho, M.J.R. Sandim, H.R.Z. Sandim, Defects in parts manufactured by selective laser melting caused by δ-ferrite in reused 316L steel powder feedstock, Addit. Manuf. 31 (2020), 100979, https://doi.org/10.1016/j.addma.2019.100979.

[28] X. Chen, X. Cheng, H. Wang, Z. Huang, Effect of heat treatment on microstructure, mechanical and corrosion properties of austenitic stainless steel 316L using arc additive manufacturing, Mater. Sci. Eng. A 715 (2018) 307–314, https://doi.org/10.1016/j.msea.2017.10.002.

[29] G.R. Mirshekari, E. Tavakoli, M. Atapour, B. Sadeghian, Microstructure and corrosion behavior of multipass gas tungsten arc welded 304L stainless steel, Mater. Des. 55 (2014) 905–911, https://doi.org/10.1016/j.matdes.2013.10.064.

[30] S. Hong, H. Kim, B.S. Kong, C. Jang, I.H. Shin, J.S. Yang, K.S. Lee, Evaluation of the thermal ageing of austenitic stainless steel welds with 10% of δ-ferrites, Int. J. Press. Vessel. Pip. 167 (2018) 32–42, https://doi.org/10.1016/j.ijpvp.2018.10.006.

[31] B. Verhaeghe, F. Louchet, B. Doisneau-Cottignies, Y. Bréchet, J.-P. Massoud, Micromechanisms of deformation of an austenoferritic duplex stainless steel, Philos. Mag. A 76 (1997) 1079–1091, https://doi.org/10.1080/01418619708200016.

[32] J.M. Torralba, J. Hidalgo, 18 - Metal injection molding (MIM) of stainless steel. Handbook of Metal Injection Molding, Second Edition, 2019, pp. 409–429, https://doi.org/10.1016/B978-0-08-102152-1.00022-2.

[33] P.A. Davies, G.R. Dunstan, R.I.L. Howells, A.C. Hayward, Aerospace adds lustre to appeal of master alloy MIM feedstocks, Met. Powder Rep. 59 (14–16) (2004) 18–19, https://doi.org/10.1016/S0026-0657(04)00277-2.

[34] D. Jiang, F. Ning, Anisotropic deformation of 316L stainless steel overhang structures built by material extrusion based additive manufacturing, Addit. Manuf. 50 (2022), 102545, https://doi.org/10.1016/j.addma.2021.102545.

[35] ASTM G61–86, Standard Test Method for Conducting Cyclic Potentiodynamic Polarization Measurements for Localized Corrosion Susceptibility of Iron-, Nickel-, or Cobalt-Based Alloys (ASTM International, 2014).

[36] ASTM-E8 (2016) Standard test methods for tension testing of metallic materials. ASTM International, West Conshohocken, PA. doi: ⟨10.1520/E0008_E0008M-16AE01⟩.

[37] S. Mirzababaei, B.K. Paul, S. Pasebani, Microstructure-property relationship in binder jet produced and vacuum sintered 316 L, Addit. Manuf. 53 (2022), 102720, https://doi.org/10.1016/j.addma.2022.102720.

[38] B. Liu, P. Eisenlohr, F. Roters, D. Raabe, Simulation of dislocation penetration through a general low-angle grain boundary, Acta Mater. 60 (2012) 5380–5390, https://doi.org/10.1016/j.actamat.2012.05.002.

[39] W. Xu, Y.C. Xin, B. Zhang, X.Y. Li, Stress corrosion cracking resistant nanostructured Al-Mg alloy with low angle grain boundaries, Acta Mater. 225 (2022), 117607, https://doi.org/10.1016/j.actamat.2021.117607.

[40] B. Berginc, Z. Kampus, B. Sustarsic, Influence of feedstock characteristics and process parameters on properties of MIM parts made of 316L, Powder Met. 50 (2007) 172–183, https://doi.org/10.1179/174329007×164862.

[41] N. Lecis, M. Mariani, R. Beltrami, L. Emanuelli, R. Casati, M. Vedani, A. Molinari, Effects of process parameters, debinding and sintering on the microstructure of 316L stainless steel produced by binder jetting, Mater. Sci. Eng. A 828 (2021), 142108, https://doi.org/10.1016/j.msea.2021.142108.

[42] A.C. Rios, E. Hryha, E. Olevsky, P. Harlin, Sintering anisotropy of binder jetted 316L stainless steel: part I – sintering anisotropy, Powder Met. 65 (2021) 273–282, https://doi.org/10.1080/00325899.2021.2020485.

[43] J. Smith, W. Xiong, J. Cao, W.K. Liu, Thermodynamically consistent microstructure prediction of additively manufactured materials, Comput. Mech. 57 (2016) 359–370, https://doi.org/10.1007/s00466-015-1243-1.

[44] P. Kumar, R. Jayaraj, J. Suryawanshi, U.R. Satwik, J. McKinnell, U. Ramamurty, Fatigue strength of additively manufactured 316L austenitic stainless steel, Acta Mater. 199 (2020) 225–239, https://doi.org/10.1016/j.actamat.2020.08.033.

[45] M. Jamalkhani, M. Asherloo, O. Gurlekce, I.-T. Ho, M. Heim, D. Nelson, A. Mostafaei, Deciphering microstructure-defect-property relationships of vacuum-sintered binder jetted fine 316L austenitic stainless steel powder, Addit. Manuf. 59 (2022), 103133, https://doi.org/10.1016/j.addma.2022.103133.

[46] A.C. Rios, E. Hryha, E. Olevsky, P. Harlin, Sintering anisotropy of binder jetted 316L stainless steel: part II – microstructure evolution during sintering, Powder Met. 65 (2021) 283–295, https://doi.org/10.1080/00325899.2021.2020486.

[47] K. Shimizu, H. Tsuruta, Y. Kamada, T. Murakami, H. Watanabe, Crystallographic analysis of Ga irradiation-induced phase transformation in austenitic stainless steels, Mater. Charact. 194 (2022), 112375, https://doi.org/10.1016/j.matchar.2022.112375.

[48] S. Mendelson, The Kurdjumov-Sachs, Bogers-Burgers, Nishiyama, and Zener models for martensite formation in FCC→BCC, Scr. Mater. 11 (1977) 375–382, https://doi.org/10.1016/0036-9748(77)90270-8.

[49] G. Monrrabal, J.A. Jiméneza, J. Ress, S. Fajardo, J.M. Bastidas, I. Llorente, Corrosion behaviour of resistance-spot-welded high-Mn austenitic TWIP steel, Corros. Eng. Sci. Technol. 56 (2021) 50–59, https://doi.org/10.1080/1478422X.2020.1806606.

[50] X. Chen, X. Cheng, H. Wang, Z. Huang, Effect of heat treatment on microstructure, mechanical and corrosion properties of austenitic stainless steel 316L using arc additive manufacturing, Mater. Sci. Eng. A. 715 (2018) 307–314, https://doi.org/10.1016/j.msea.2017.10.002.

[51] G.R. Mirshekari, E. Tavakoli, M. Atapour, B. Sadeghian, Microstructure and corrosion behavior of multipass gas tungsten arc welded 304L stainless steel, Mater. Des. 55 (2014) 905–911, https://doi.org/10.1016/j.matdes.2013.10.064.

[52] C.T. Kwok, S.L. Fong, F.T. Cheng, H.C. Man, Pitting and galvanic corrosion behavior of laser-welded stainless steels, J. Mater. Process. Technol. 176 (2006) 168–178, https://doi.org/10.1016/j.jmatprotec.2006.03.128.

[53] C. Carboni, P. Peyre, G. Béranger, C. Lemaitre, Influence of high power diode laser surface melting on the pitting corrosion resistance of type 316L stainless steel, J. Mater. Sci. 37 (2002) 3715–3723, https://doi.org/10.1023/A:1016569527098.

[54] J. Wang, H. Su, K. Chen, D. Du, L. Zhang, Z. Shen, Effect of δ-ferrite on the stress corrosion cracking behavior of 321 stainless steel, Corros. Sci. 158 (2019), 108079, https://doi.org/10.1016/j.corsci.2019.07.005.

[55] Z. Zhang, Z. Zhao, X. Li, L. Wang, B. Liu, P. Bai, Effect of heat treatments on metastable pitting of 316L stainless steel fabricated by selective laser melting, J. Mater. Res. Technol. (2022), https://doi.org/10.1016/j.jmrt.2022.10.039.

[56] K. Wang, Q. Chao, M. Annasamy, P.D. Hodgson, S. Thomas, N. Birbilis, D. Fabijanic, On the pitting behaviour of laser powder bed fusion prepared 316L stainless steel upon post-processing heat treatments, Corros. Sci. 197 (2022), 110060, https://doi.org/10.1016/j.corsci.2021.110060.

[57] G. Luo, H. Xiao, S. Li, C. Wang, Q. Zhu, L. Song, Quasi-continuous-wave laser surface melting of aluminium alloy: precipitate morphology, solute segregation and corrosion resistance, Corros. Sci. 152 (2019) 109–119, https://doi.org/10.1016/j.corsci.2019.01.035.

[58] Q. Chao, S. Thomas, N. Birbilis, P. Cizek, P.D. Hodgson, D. Fabijanic, The effect of post-processing heat treatment on the microstructure, residual stress and mechanical properties of selective laser melted 316L stainless steel, Mater. Sci. Eng. A. 821 (2021), 141611, https://doi.org/10.1016/j.msea.2021.141611.

[59] A. Röttger, K. Geenen, M. Windmann, F. Binner, W. Theisen, Comparison of microstructure and mechanical properties of 316 L austenitic steel processed by selective laser melting with hot-isostatic pressed and cast material, Mater. Sci. Eng. A. 678 (2016) 365–376, https://doi.org/10.1016/j.msea.2016.10.012.

[60] A.B. Kale, B.K. Kim, D.I. Kim, E.G. Castle, M. Reece, S.H. Choi, An investigation of the corrosion behavior of 316L stainless steel fabricated by SLM and SPS techniques, Mater. Charact. 163 (2020), 110204, https://doi.org/10.1016/j.matchar.2020.110204.

[61] S.M. Yusuf, M. Nie, Y. Chen, S. Yang, N. Gao, Microstructure and corrosion performance of 316L stainless steel fabricated by selective laser melting and processed through high-pressure torsion, J. Alloy. Compd. 763 (2018) 360–375, https://doi.org/10.1016/j.jallcom.2018.05.284.

[62] ASTM-A240 (2020) Standard specification for chromium and chromium-nickel stainless steel plate sheet and strip for pressure vessels and for general applications. ASTM International, West Conshohocken, PA. doi: ⟨10.1520/A0240_A0240M-20A⟩.